International Journal of Nanomedicine

Dovepress

open access to scientific and medical research

Open Access Full Text Article

ORIGINAL RESEARCH

Combined Ferritin Nanocarriers with ICG for Effective Phototherapy Against Breast Cancer

Leopoldo Sitia[1,*], Paola Saccomandi[2,*], Leonardo Bianchi[2], Marta Sevieri[1], Cristina Sottani[3], Raffaele Allevi[1], Elena Grignani[3], Serena Mazzucchelli[1], Fabio Corsi[1,4]

[1]Department of Biomedical and Clinical Sciences, Università degli studi di Milano, Milan, Italy; [2]Department of Mechanical Engineering, Politecnico di Milano, Milan, Italy; [3]Environmental Research Center, Istituti Clinici Scientifici Maugeri IRCCS, Pavia, Italy; [4]Istituti Clinici Scientifici Maugeri IRCCS, Pavia, Italy

*These authors contributed equally to this work

Correspondence: Serena Mazzucchelli, Department of Biomedical and Clinical Sciences, Università degli studi di Milano, via G.B. Grassi 74, Milan, 20157, Italy, Email serena.mazzucchelli@unimi.it; Fabio Corsi, Istituti Clinici Scientifici Maugeri IRCCS, via S. Maugeri 10, Pavia, 27100, Italy, Email fabio.corsi@unimi.it

Introduction: Photodynamic Therapy (PDT) is a promising, minimally invasive treatment for cancer with high immunostimulatory potential, no reported drug resistance, and reduced side effects. Indocyanine Green (ICG) has been used as a photosensitizer (PS) for PDT, although its poor stability and low tumor-target specificity strongly limit its efficacy. To overcome these limitations, ICG can be formulated as a tumor-targeting nanoparticle (NP).

Methods: We nanoformulated ICG into recombinant heavy-ferritin nanocages (HFn-ICG). HFn has a specific interaction with transferrin receptor 1 (TfR1), which is overexpressed in most tumors, thus increasing HFn tumor tropism. First, we tested the properties of HFn-ICG as a PS upon irradiation with a continuous-wave diode laser. Then, we evaluated PDT efficacy in two breast cancer (BC) cell lines with different TfR1 expression levels. Finally, we measured the levels of intracellular endogenous heavy ferritin (H-Fn) after PDT treatment. In fact, it is known that cells undergoing ROS-induced autophagy, as in PDT, tend to increase their ferritin levels as a defence mechanism. By measuring intracellular H-Fn, we verified whether this interplay between internalized HFn and endogenous H-Fn could be used to maximize HFn uptake and PDT efficacy.

Results: We previously demonstrated that HFn-ICG stabilized ICG molecules and increased their delivery to the target site in vitro and in vivo for fluorescence guided surgery. Here, with the aim of using HFn-ICG for PDT, we showed that HFn-ICG improved treatment efficacy in BC cells, depending on their TfR1 expression. Our data revealed that endogenous H-Fn levels were increased after PDT treatment, suggesting that this defence reaction against oxidative stress could be used to enhance HFn-ICG uptake in cells, increasing treatment efficacy.

Conclusion: The strong PDT efficacy and peculiar Trojan horse-like mechanism, that we revealed for the first time in literature, confirmed the promising application of HFn-ICG in PDT.

Keywords: heavy-ferritin nanocages, indocyanine green, photodynamic therapy, breast cancer, tumor-targeted nanoparticles

Introduction

Photothermal and photodynamic therapy (PTT and PDT, respectively) represent promising approaches in cancer therapy, aimed at reducing side effects, minimizing invasiveness, and overcoming drug resistance.[1] These techniques rely on the use of specific molecules, known as photosensitizers (PSs), which generate heat (PTT) or release cytotoxic substances (PDT) when exposed to an external source of energy.[2,3] PTT and PDT employ a light laser to excite PSs at specific wavelengths. The potential advantages of PTT and PDT include high antitumor efficacy with a minimally invasive approach, extremely low toxicity in surrounding healthy tissues, and no reported insurgence of resistance mechanisms.[4] Among the different classes of PSs to have been proposed, the first ones were porphyrins and their derivatives.[5] However, major drawbacks were reported in different clinical trials in relation to porphyrin-related PSs, such as slow excretion, high bioaccumulation and strong adverse reactions to visible light.[6] A particularly interesting PS is Indocyanine Green (ICG). ICG is an FDA approved fluorescent dye that is currently used in

Received: 18 October 2023
Accepted: 30 March 2024
Published: 14 May 2024

Graphical Abstract

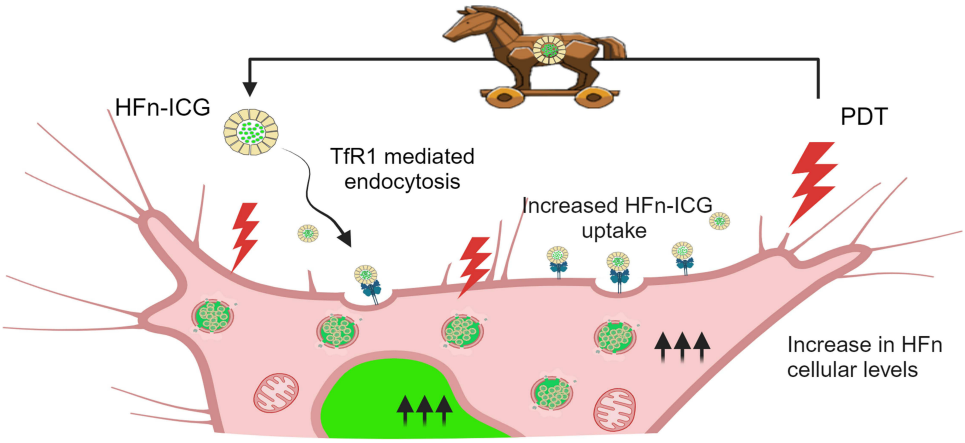

oncology to track sentinel lymph nodes in breast cancers (BCs) and is widely adopted in laparoscopic surgery to enhance visibility and provide detailed anatomical information during surgery.[7] More recently, ICG has also been tested as a PS for PTT and PDT. Thanks to its optical response in the near-infrared (NIR) spectrum, at which light absorption by tissues is minimal, it allows the high laser penetration that is required to treat deeply located tumors.[8] When irradiated, ICG generates heat, and even more interestingly, it reacts with the molecular oxygen found in tissues, thus producing reactive oxygen species (ROS).[9] These activate a series of intracellular toxic reactions such as endoplasmic reticulum stress and DNA damage that induce apoptosis.[6] Dying cancer cells release several factors that induce an immune response within the organism, the so-called immunogenic cell death (ICD). Therefore, ICG-based PDT has been used in combination with immunotherapy, demonstrating a strong synergistic effect.[1,10]

Despite the advantages of ICG, a drawback to its application in PDT has been its rapid metabolism and degradation, which significantly limits tumor targeting and accumulation and strongly reduces its efficacy as a PS.[11] To overcome these limitations and to prolong its half-life, ICG has been encapsulated in engineered nanoparticles (NPs). However, most ICG nanoformulation strategies exploit the so-called enhanced permeability and retention (EPR) effect and are therefore well suited to improve passive ICG accumulation in tumors. The design of a proper tumor-targeting nanoformulation would significantly improve the local accumulation of ICG and its PDT efficacy.[6]

In this study, we propose the use of recombinant heavy-ferritin nanocages (HFn) to nanoformulate ICG with the aim of increasing its PDT potential application for BC, exploiting HFn natural tumor homing ability.[12] HFn is 12 nm hollow spherical nanocage derivatives of ferritin (Fn), a ubiquitous human protein involved in iron homeostasis. HFn consist of 24 monomers of the H-chain of Fn characterized by a high thermal stability and low immunogenicity, as already reported by different groups, including ours.[13–15] Moreover, HFn can be loaded with drugs and fluorescent dyes for theranostic applications, following different approaches. The most common ones are the disassembly-reassembly induced by pH variation or by incubation with urea, and the opening of peculiar loading channels by increasing the temperature of the HFn solution.[16,17] Furthermore, as observed for the native protein, HFn follows a specific cellular uptake mechanism mediated by the interaction with transferrin receptor 1 (TfR1).[18,19] As reported by the Human Protein Atlas, TfR1 is a cytoplasmic and membranous receptor whose expression is normal in most tissues and slightly abundant in placental and bone marrow cells.[20,21] In addition, TfR1 is highly overexpressed in most cancers where it is strongly correlated with an unfavorable prognosis.[22–24] All these properties make HFn a promising theranostic delivery agent in many types of cancer. HFn has been widely used for tumor-targeted delivery in chemotherapy and immunotherapy.[25–27] Moreover, we already showed that, by loading ICG into HFn (HFn-ICG), we could specifically deliver the encapsulated dye in cancer cells and identify the neoplastic tissues for fluorescence guided surgery.[11,28,29]

Another interesting aspect of Fn is its involvement in cell homeostasis during particular cell stress such as ferroptosis and ROS-induced autophagy. This is a defence mechanism that cells activate in response to oxidative stress induced by external stimuli. Fn has potent ferroxidase activity that catalyzes the oxidation of ferrous iron, protecting the nuclei from free radicals in cells exposed to oxidative stress.[30,31] Moreover, it has been reported that TfR1 expression levels also increase during ferroptosis.[32] These mechanisms have never been proven in PDT. We previously showed that incubation with doxorubicin-loaded HFn increased intracellular Fn levels and nuclear translocation.[33] We used this reaction to significantly increase HFn uptake in tumor cells. Here, for the first time in literature, we showed that ICG treatment and irradiation resulted in a significant overexpression of the intracellular levels of endogenous H-ferritin (H-Fn) and its nuclear translocation, leading to a higher uptake of the exogenous HFn. Interestingly, this higher need of Fn in stressed cells could be turned from a defence mechanism to a "Trojan horse" mechanism used to significantly increase HFn intracellular delivery, thus strongly supporting the use of HFn-ICG for PDT in tumors.

Materials and Methods

BT-474 invasive ductal carcinoma and HCC1937 primary ductal carcinoma BC cell lines were purchased from American Type Culture Collection-Laboratory of the Government Chemist (ATCC-LGC) and were cultured in Dulbecco's Modified Eagle Medium High Glucose (DMEM HG) medium and Roswell Park Memorial Institute (RPMI) 1640 Medium, respectively, supplemented with 10% heat inactivated fetal bovine serum (FBS), 2 mM l-glutamine, 100 U/mL penicillin, and 0.1 mg/mL streptomycin. Both cell lines grew at 37 °C in a humidified atmosphere containing 5% CO_2 and were subcultured prior to confluence using trypsin/ethylenediaminetetraacetic acid (EDTA). The cell culture medium and chemicals for cell culture were purchased from Euroclone (Pero, Italy).

Set Up of Laser Irradiation and Study of Temperature Effects

NIR laser irradiation experiments were performed by exposing each sample to an 808 nm continuous-wave diode laser (LuOcean Mini 4, Lumics, Berlin, Germany) in one well of a transparent 24-well plate (24 MW), without any cover. The NIR radiation was delivered in a contactless manner. The laser emitter was connected to a 400-µm core diameter quartz optical fiber (OZ Optics Ltd., Ottawa, Canada), which was connected to a collimator orthogonally positioned above the 24 MW and 11 cm from the bottom of the plate itself. This height was chosen such that the laser beam spot size covered the entire surface of a well of 24 MW used for the experiments. For each sample, irradiation was performed with a laser power of 2.1 W (power density of approximately 1 W/cm^2) and exposure time of 3 minutes (min). These values were selected according to existing literature.[34–37] Real-time thermographic imaging was used to monitor the temperature during irradiation. Images were captured at 10 frames per second (fps) using an infrared thermographic camera (FLIR System, T540 with 464 × 348 pixels spatial resolution, ±2 °C accuracy). For the thermal analysis, a region of interest (ROI) corresponding to the sample area was defined in each thermographic image, and the average temperature values over time were extracted for each ROI.

Evaluation of ICG Phototherapy: Cytotoxicity and Intracellular Heavy-Ferritin (H-Fn) Production

To verify the photothermal effect of ICG and establish optimal experimental conditions, BT-474 cells were seeded into the 24 MW at a concentration of 2×10^4 cells/well and allowed to adhere for 24 hours (h). ICG was diluted into the culture medium at final concentrations of 5, 10, and 50 µg/mL and then incubated with cells for 24 h. At the end of the incubation, ICG was removed, and cells were washed three times with phosphate buffered saline (PBS) to remove non-internalized dye and incubated with fresh culture medium. Cells were then irradiated with the laser at a power of 1W/cm^2 for three min and the temperature trends were measured during irradiation. After irradiation, cells were placed back in the incubator for 24 h. Cells were gently detached from the wells and incubated with MTS solution (1:5 dilution with phenol red-free medium, 96 MW for 3 h, n = 7). The viability of ICG-incubated irradiated and non-irradiated cells was compared with that of non-incubated non-irradiated control cells.

To unveil the cellular adaptive mechanisms induced by laser irradiation in ICG-treated cells, endogenous H-Fn production and intracellular localization were monitored. Cells were treated with 10 µg/mL ICG for 24 h, irradiated as described previously, and placed back in the incubator. Three and 24 h later, irradiated cells were washed with PBS, fixed with 4% paraformaldehyde (PFA)

solution for 10 min at room temperature (RT), and permeabilized with a Triton X-100 0.1% solution 5 min RT. Endogenous H-Fn was stained with an anti-H-Fn primary antibody (ab7332, Abcam, 1:2000 in 2% Bovine Serum Albumin (BSA), 2% Goat Serum (GS), overnight (O/N), 4 °C), followed by incubation with a secondary antibody (A-11010, goat anti-rabbit Alexa-Fluor 546 (AF546), Thermo Fisher Scientific, 1:1000, 2 h, RT) and nuclear staining with 4′,6-diamidino-2-phenylindole (DAPI) (1:200, PBS, 10 min, RT). To quantify the intracellular levels of H-Fn, at least 10 confocal microscopy images/condition were analyzed (SP8, Leica Microsystems, 63 × magnification oil objective). Nuclear and cellular masks were built using ImageJ, and the intensity of the H-Fn-related fluorescence signal was calculated in the nucleus and cytoplasm (as the total cellular minus the nuclear signal). Untreated irradiated cells were used to calculate the H-Fn induction signal due to simple laser irradiation.

HFn Preparation and Characterization

Highly stable and endotoxin-free HFn was produced as a recombinant protein following a protocol that we have recently optimized.[13] Briefly, the pET11a/HFn plasmid was subcloned into ClearColi® BL21 (DE3) (Lucigen, LGC Ltd, UK) plated onto LB-Miller agar-coated dishes and grown O/N to obtain cell colonies. A single colony was grown in LB-Miller broth O/N and further subcultured until an OD_{600nm} of 0.6 was reached. Gene expression was induced by incubating the cells with 0.5 mM isopropyl β-d-1-tiogalactopiranoside (IPTG, cat n. I1284, Sigma-Aldrich) O/N. At the end of incubation, cells were harvested by centrifugation (two cycles, 4000 × *g* for 15 min at 4 °C), re-suspended in physiological buffer (10 mM K_2HPO_4, 1.8 mM KH_2PO_4, 150 mM NaCl, pH 7.2), and lysed in lysis buffer (20 mM KMES pH 6.0, 1mM phenylmethanesulfonyl fluoride, complete EDTA-free protease inhibitors (50×), 1mg/mL lysozyme, and 20 mM $MgCl_2$; 3 mL/g of cells) by sonication. HFn was extracted from lysed cells by centrifugation (10,000 × *g* for 30 min at 4 °C), subjected to a 70 °C heat shock for 20 min, centrifuged again, and purified by ion-exchange chromatography using a diethylaminoethyl cellulose (DEAE) sepharose resin (cat#DCL6B100, Sigma-Aldrich). Endotoxins (LPS) were efficiently removed by incubating HFn with two cycles of Triton X-114 at a 1% v/v concentration in 15 mL tubes, following the protocol already described.[38] The concentration and the purity of the different fractions were evaluated by absorbance reading at 280 nm and by polyacrylamide gel electrophoresis (SDS-PAGE, 12% gel with Coomassie brilliant blue protein stainer), respectively. The physicochemical properties and morphology of the HFn nanocages were evaluated using transmission electron microscopy (TEM, Tecnai Spirit, FEI, magnification 300,000 ×) after staining with uranyl-acetate (1% for 30 seconds (s) at RT). Finally, LPS content was evaluated using the Limulus Amebocyte Lysate (LAL) kinetic turbidimetric assay following the manufacturer's instructions (Charles River Microbial Solutions Ltd., Dublin, Ireland).

HFn-ICG Loading and Photothermal Properties

ICG was loaded into HFn following the method we recently set up and optimized, based on the disassembly-reassembly properties of HFn in response to pH variations.[11] Briefly, the HFn solution (0.5 mg/mL, 0.15 M NaCl) was brought to pH 2.0 and incubated for 15 min at RT on an orbital shaker. ICG powder (Verdye; Diagnostic Green GmbH, Aschheim-Dornach, Germany) was dissolved in distilled water (5 mg/mL). The pH was adjusted to 7.0, allowing HFn reassembly, and ICG was immediately added to a final concentration of 1 mg/mL. The HFn-ICG solution was adjusted to a pH of 7.5 and incubated on an orbital shaker for 2 h at RT. HFn-ICG was concentrated using centrifugal filter units (Amicon Ultra-4100 kDa MWCO, Merck S.p.a., Milan, Italy, Catalog Number: UFC810024), and the non-encapsulated dye was removed by gel filtration (Zeba Spin Desalting column, Thermo Fisher Scientific, Monza, Italy; Catalog Number: 89,890). The final ICG concentration was estimated after extracting ICG from HFn (1:5 dilution in acetonitrile, 10 min centrifugation 10,000 × g, 4 °C) using a proper calibration curve prepared in milk. The ICG loading capacity (LC) was estimated by evaluating the ICG to ICG: HFn mass ratio (%) in the final preparation, as described in the literature.[39,40] Full HFn-ICG characterization including encapsulation efficiency, drug release and NP stability are reported in the cited manuscript.[11]

The loaded HFn-ICG nanocages were diluted to a final dye concentration of 20 µg/mL in PBS and irradiated with an 808 nm laser (1W/cm^2, 3 min). Temperature trends were recorded 10 s before, during, and up to 20 s after irradiation.

HFn-ICG Binding, Uptake and Biocompatibility

BT-474 cells were grown in cell culture flasks until they reached confluence. For binding studies, cells were detached, re-suspended in flow cytometry tubes (5 × 10^5 cells/tube), and incubated with different HFn-ICG and

ICG concentrations (2, 5, 10, and 20 µg/mL) for 1h at 4 °C. At the end of incubation, tubes were centrifuged (400 × *g*, 5 min, 4 °C), washed in PBS, and analyzed by flow cytometry. For uptake studies, cells were seeded into 24 MW at a density of 2×10^4 cells/well, allowed to adhere for 24 h, and incubated with 2, 5, 10, and 20 µg/mL of HFn-ICG or ICG for 1 h at 37 °C. At the end of the incubation, the cells were washed with PBS, detached, and analyzed by flow cytometry. The results are expressed as the mean fluorescence intensity and percentage of positive cells in the gated cell population (mean ± standard deviation of three independent experiments).

To assess cytotoxicity, HFn-ICG was incubated with 2×10^4 cells/well in 24 MW at equivalent ICG concentrations of 5, 20, and 50 µg/mL for 24 h. Cytotoxicity was evaluated by MTS as previously described.

Irradiation of HFn-ICG Incubated Cells and Cytotoxicity Assessment

Cells (BT-474 and HCC1937) were seeded into 24 MW (2×10^4 cells/well), allowed to adhere for 24 h, and then incubated with different concentrations of HFn-ICG and free ICG (10 and 20 µg/mL in culture medium). After 24 h of incubation, the compounds were removed, cells were washed with PBS, and fresh culture medium was added. The cells were irradiated (1 W/cm^2, 3 min per well), and the temperature trends were monitored. After irradiation, cells were returned to the incubator for 24 h, and cytotoxicity was evaluated by MTS assay and cytofluorimetry (7AAD marker) to assess metabolic dysfunction and cell death, respectively.

In another set of experiments, H-Fn expression was evaluated after irradiation. Both cell lines were seeded on collagen-coated sterile round glass slides placed inside 24 MW (2×10^4 cells/well) and incubated with ICG and HFn-ICG (10 µg/mL dye concentration) for 24 h. After incubation, cells were washed, irradiated (1 W/cm^2, 3 min), and placed in the incubator. Three and 24 h after irradiation, the cell morphology was visualized using a bright-field light microscope (three images per well in different areas). The cells were then fixed, H-Fn was stained by immunofluorescence as described above, and confocal microscopy images were acquired (10 images/well). H-Fn expression was measured in untreated, non-irradiated, and irradiated cells. The mean fluorescence intensity (M.F.I.) of H-Fn was measured in the nuclei and cytoplasm after segmentation using ImageJ as described above.

Critical Analysis of ICG After Irradiation Using UHPLC-MS/MS

The molecular characteristics of ICG before and after irradiation were studied using ultra-high-performance tandem mass spectrometry (UHPLC-MS/MS).

Freshly prepared solutions of ICG and HFn-ICG were obtained at a dye concentration of 10 µg/mL and were irradiated (1 W/cm^2, 3 min) in 24 MW. The solutions were collected immediately and frozen for further analysis.

For the assessment of ICG and HFn-ICG degradation peaks, electrospray ion source tandem mass spectrometry (ESI-MS/MS) was used and operated in positive mode (ESI+) using Agilent Jet Stream technology. Ion source parameters were as follows: 11 mL/min, 300 °C vaporizer temperature, 300 °C sheath gas, 600 V nozzle voltage, and 3000 V capillary voltage. Nitrogen was used as the nebulizer gas at 45 psi, with a flow rate of 5 L/min. The instrument consisted of an Agilent 1290 Infinity Binary Pump, a 1290 Infinity Sampler, and a 1290 Infinity Thermostat. The UHPLC system was interfaced with an Agilent 6460 triple-quadrupole mass spectrometer (Agilent Technologies, Lexington, CA, USA). The Mass Hunter workstation was used for data acquisition and analysis (Version 10.1 2006–2020).

The analysis was performed using a Waters Acquity UPLC HSS T3 column (1.8 µm, 2.1 mm × 100 mm, Waters, Milford, MA, USA) maintained at 40 °C with a flow rate of 0.3 mL/min. The MS/MS measurements used collision-induced dissociation (CID) in a closed-design Q2 collision cell operating at a collision energy voltage (V) of 40, a cell-accelerated voltage of 4, and a fragmentor voltage of 215.

ESI-MS/MS experiments were performed in both the ESI-MS and ESI-MS/MS modes to acquire the protonated molecular ion $[MH]^+$ of ICG at m/z 753.0 and the product ions of the parent compound. The samples were analyzed using a previously described gradient program to elute ICG with a retention time (Rt) of 3 min.[41]

Statistical Analysis

All experiments were performed in triplicate, except when indicated otherwise. The results are expressed as the average ± standard deviation. Statistical analysis was performed using GraphPad 8.0 (GraphPad Software, San Diego, CA, USA)

with one-way analysis of variance and paired Student's *t*-test after verifying data normality. Differences were considered to be statistically significant at $p \leq 0.05$.

Results and Discussion

ICG is a safe fluorescent dye with PS properties that can convert light energy into heat, induce apoptosis and reactive oxygen species (ROS) production in many types of irradiated cancer cells.[42,43] As shown in Figure 1a, ICG safety was first confirmed by measuring cell viability in non-irradiated cells incubated with up to 50 μg/mL dye (ICG^-, empty squares). Then, to establish the best PDT conditions in BT-474 BC cells, we evaluated the cytotoxicity and thermal response of irradiated cells incubated with different concentrations of ICG. In contrast with untreated-irradiated cells, ICG-treated and irradiated cells (ICG^+, full dots) showed relevant cytotoxicity starting at 10 μg/mL after 3 min of irradiation with 1 W/cm^2 laser power. These parameters, which are in line with what other authors have used for PDT with ICG,[36,37] were selected to maintain a good balance between irradiation time and laser power: they guarantee a fast treatment without the risk of generating off target side effects related to a strong laser intensity.[44] Temperature trends acquired in irradiated cellsshowed that, even in the cells where intracellular ICG induced a strong cytotoxicity after irradiation (cells treated with 50 μg/mL of ICG), the temperature rose to a maximum average value of 30.5 °C, with an increase of only 4.8 °C (Figure 1b and Table 1). This suggested to us that the observed toxicity was due to a photodynamic effect rather than a photothermal one, which usually occurs when the temperature is maintained above 42–47 °C for several minutes.[45] This prompted us to investigate the molecular alterations that occur intracellularly during PDT and to find an appropriate delivery vehicle capable of guaranteeing a more efficient ICG tumor accumulation.[28]

Starting from the observation that PDT causes the release of ROS, that intracellular Fn levels are increased during treatments that increase oxidative stress, and that a stress-dependent nuclear translocation of both Fn and recombinant HFn have been observed,[31,46,47] we reasoned that HFn could be an extremely good ICG delivery vehicle for PDT. Indeed, our group has already demonstrated that, because of this stress-dependent nuclear translocation, HFn loaded with doxorubicin mediates the direct nuclear delivery of the cargo, by exploiting a "Trojan horse"-like mechanism that boosts HFn intracellular uptake. This evidence prompted us to assess the reliability of HFn as a "Trojan horse" vehicle for the delivery of ICG for PDT. First, we evaluated whether ICG uptake coupled with irradiation was sufficient to cause an increase in Fn expression and to trigger its nuclear translocation. Using immunofluorescence, we measured intracellular levels of the endogenous H-Fn in ICG-treated and irradiated cells. As shown in Figure 1c–e, the overall cellular H-Fn signal (reported in green) was significantly increased ($p < 0.0001$) in cells incubated with ICG 3 and 24 h after irradiation (ICG^+ 3h, ICG^+ 24h), as compared to non-irradiated cells (ICG^- 3h, ICG^- 24h). A non-significant increase in H-Fn was also observed in irradiated control cells (not pre-incubated with ICG) 24 h after irradiation (CTR^+ 24h). This suggested that the laser might disturb cell homeostasis without hampering cell viability, as demonstrated by MTS data of irradiated untreated cells (first ICG^+ black dot near the y axis, at 0 μg/mL of dye, Figure 1a).

These data represent a major novelty in the field of phototherapy and prompted us to use HFn to deliver ICG intracellularly by exploiting this peculiar translocation mechanism activated after laser irradiation. To do so, we applied a protocol we recently developed to encapsulate ICG into HFn, by using a new formulation of endotoxin-free protein with the advantage of opening the way for potential further studies in vivo.[11,13] This protocol exploits the unusual HFn stability at extreme pH values and its natural capability to disassemble-reassemble its quaternary structure in response to pH variations.[11] In a recent manuscript, aimed at using HFn-ICG for fluorescence guided surgery,[11] we had already reported major HFn-ICG characterization, including encapsulation efficiency and ICG release. For this reason, in the present manuscript aimed at evaluating HFn-ICG use in PDT, we have repeated only novel characterization of the loaded nanocages, as described below. First, by TEM, we verified that after encapsulation of ICG, HFn retained its nanocage structure with an approximate diameter of 12 nm and an inner core of 8 nm (Figure 2a), preserving also the correct monomer molecular weight of approximately 20 kDa (Figure 2b).[48] Then, we verified that endotoxins were efficiently removed from the protein, down to a value of 0.31 EU/mg as imposed by the regulatory agencies for parenterally administered compounds.[49] We evaluated the ICG loading capacity (LC) by measuring the quantity of ICG per HFn and found a mass-to-mass ratio of 96 ± 16%.

We then compared the temperature trends of two solutions of HFn-ICG and free ICG in response to irradiation, and found that, at corresponding dye concentrations (20 μg/mL), irradiation of HFn-ICG led to a much higher temperature increase than the one registered for ICG alone (Figure 2c). Moreover, free ICG reached its peak temperature after the first minute of irradiation,

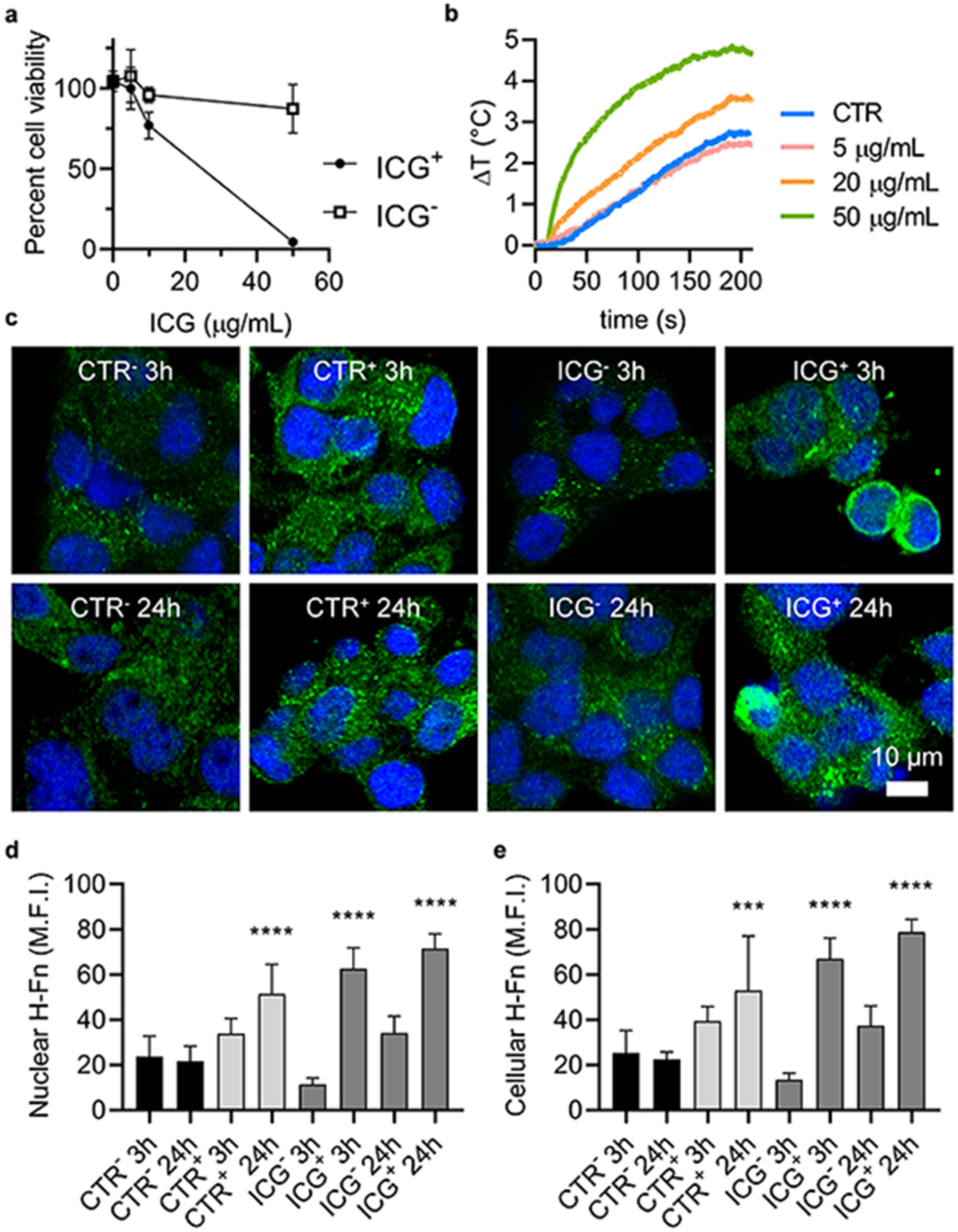

Figure 1 Viability of untreated (ICG^-) and ICG treated (ICG^+) BT-474 cells after irradiation with an 808 nm diode laser ($1W/cm^2$, 3 min irradiation) measured by MTS assay 24 h after irradiation (**a**); temperature trends of BT-474 cells during irradiation in untreated (CTR) cells and after incubation with ICG at increasing concentrations (**b**); representative confocal microscopy images of untreated non-irradiated (CTR^-), untreated irradiated (CTR^+), ICG treated non-irradiated $(ICG)^-$ and ICG treated irradiated (ICG^+) cells obtained 3 h and 24 h after ICG treatment and/or irradiation. H-Fn expression was evaluated by immunofluorescence analysis (green: H-Fn signal; blue: nuclei signal) (**c**); quantification of H-Fn signal in cell nuclei (**d**) and cytoplasm (**e**) after segmentation with ImageJ of 10 images/condition. Statistical analysis was done by ordinary one-way ANOVA against relative CTR groups. ***p<0.001, ****p<0.0001.

Table 1 Temperature Data of Irradiated BT-474 Cells Treated with Increasing Concentrations of ICG

Sample	T_{in} (°C)	T_{max} (°C)	ΔT_{max} (°C)
CTRL	24.4 ± 0.5	27.2 ± 0.6	2.8 ± 0.3
ICG 5 μg/mL	25.1 ± 1.1	27.6 ± 0.8	2.5 ± 0.3
ICG 10 μg/mL	23.0 ± 0.3	26.8± 0.4	3.5 ± 0.4
ICG 20 μg/mL	24.2 ± 0.2	27.8 ± 0.1	3.6 ± 0.2
ICG 50 μg/mL	25.6 ± 0.2	30.5 ± 0.3	4.8 ± 0.2

when it reached a plateau. In contrast, the HFn-ICG temperature continued to increase for the entire three minutes of analysis and failed to reach a plateau. This might be due to the "protective" effect of HFn, which could slow the degradation of the dye, as already shown by us when using HFn-ICG for fluorescence-guided tumor targeting, and by others during irradiation.[11,50]

To test its safety and interactions with cells, we incubated HFn-ICG with BT-474 cells and found that it did not affect cell viability at concentrations up to 50 μg/mL (Figure 3a). Moreover, the nanoformulation of ICG allowed a significantly higher binding and uptake compared to the free dye in terms of mean fluorescence intensity (M.F.I.), with percentages of positively stained cells approximating 100% (Figure 3b and c, Figure S1), most likely because of the specific interaction of HFn with TfR1, which is particularly overexpressed in BT-474 cells.

Having verified the potential of HFn as an ICG nanocarrier, we tested its photodynamic effect in two BC cell lines, BT-474 and HCC1937, which are characterized by high and mild TfR1 overexpression, respectively. We focused on two dye concentrations where only a mild temperature increase was observed with the concomitant insurgence of a significant cytotoxic photodynamic effect (Figure 1a and b).

As shown in Figure 4a and b, HFn-ICG and ICG led to similar temperature increase trends, with a slight difference for HFn-ICG in TfR1-high BT-474 cells at a concentration of 20 μg/mL. In all cases, we measured a relatively low-temperature increase, with a maximum ΔT of approximately 5 °C and maximum temperature of 29.1 °C (Table 2). These data confirm what was previously observed in ICG-treated cells at similar concentrations.

Next, we studied cell viability upon irradiation. In BT-474, significant differences between HFn-ICG and ICG were observed for both 10 and 20 μg/mL treatments, with percentages of viable cells measured by MTS assay of 40 and 10% with HFn-ICG as compared with 90 and 60% with ICG, respectively (Figure 4c). Similar statistically significant differences were observed by cytofluorimetry when measuring cell death using the 7-AAD marker (Figure 4e). In

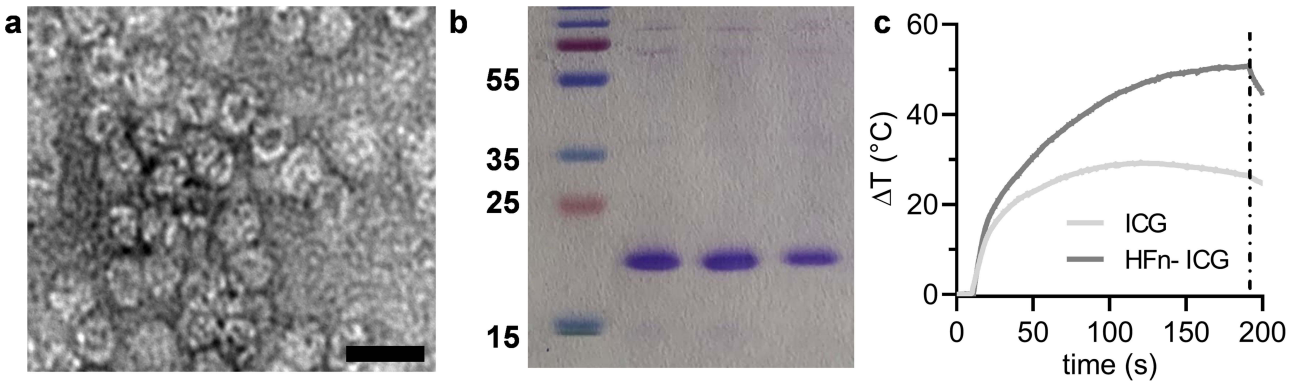

Figure 2 HFn-ICG characterization by TEM, scale bar 20 nm (**a**), SDS gel electrophoresis showing the band from three different HFn-ICG replicates between 20 and 25 kDa (**b**), and temperature increase (ΔT) of two solutions of HFn-ICG and free ICG (20 μg/mL equivalent dye concentration) during irradiation with an 808 nm diode laser (1W/cm^2, 3 min) (**c**).

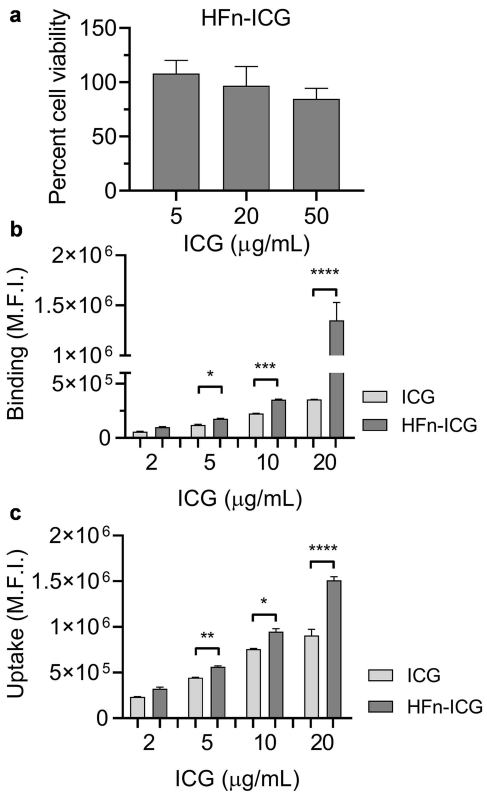

Figure 3 Cell viability measurement in BT-474 cells incubated with different concentrations of HFn-ICG (24 h incubation) at different concentrations (**a**); binding and cellular uptake in BT-474 cells incubated with different concentrations of ICG and HFn-ICG for 1 h at 4 °C (binding) and 1 h at 37 °C (uptake) (**b** and **c**). M.F.I.= Mean Fluorescence Intensity. Statistical analysis was done by ordinary one-way ANOVA. *p<0.05, **p<0.01, ***p<0.001, ****p<0.0001.

HCC1937 cells instead, the only significant difference between free and nanoformulated ICG was observed at a concentration of 20 μg/mL 24 h after irradiation (Figure 4d and f, Table 3). This strongly suggests that TfR1 expression plays a key role in regulating the interactions between HFn-ICG and cells and regulating the efficacy of HFn-ICG as PS. Highly TfR1 expressing cells have higher interactions with HFn-ICG that led to a significant increase in treatment efficacy. By correlating the strong cytotoxicity data despite the relatively low-temperature increase observed during irradiation, we confirmed that at the tested concentrations, both ICG and HFn-ICG had an exclusive photodynamic effect, most likely due to the dye degradation. This could be enormously advantageous in limiting the potential temperature-related side effects observed during PTT in vivo.

To confirm the photodynamic effect and further strengthen the rationale for using HFn-ICG for PDT, we evaluated H-Fn intracellular expression in cells treated with ICG and HFn-ICG at an equivalent dye concentration of 10 μg/mL. Interestingly, 3 h after irradiation, H-Fn expression was significantly increased in the nuclei of BT-474 cells treated with HFn-ICG compared to those treated with ICG (Figure 5a and b). Only an increased trend was observed in the cell H-Fn levels. No significance was observed in HCC1937 cells 3 h after irradiation (Figure 5d–f), suggesting slower uptake kinetics due to the lower TfR1 expression levels. Here, H-Fn was significantly increased only 24 h later both in the nuclei and in the cytoplasm. This suggests that the TfR1-mediated interaction of HFn with cells drives faster and higher HFn intracellular uptake, which helps to accelerate HFn-mediated photodynamic effects, as observed in the cytotoxicity data (Figure 4c and e). The nuclear/cell ratio remained similar in both cell lines throughout the duration of the analysis, suggesting that H-Fn production follows a dynamic process where H-Fn nuclear translocation is immediately followed by the synthesis or uptake of new H-Fn (Figure S2a and b). A detailed evaluation of the intracellular distribution of H-Fn is shown in Figure S3 and S4, where single fluorescence channels are reported.

The morphology of ICG- and HFn-treated cells was evaluated by bright-field light microscopy 3 and 24 h after irradiation to further correlate H-Fn production with evidence of cytotoxicity. As shown in Figures S5 and S6, 3 h after

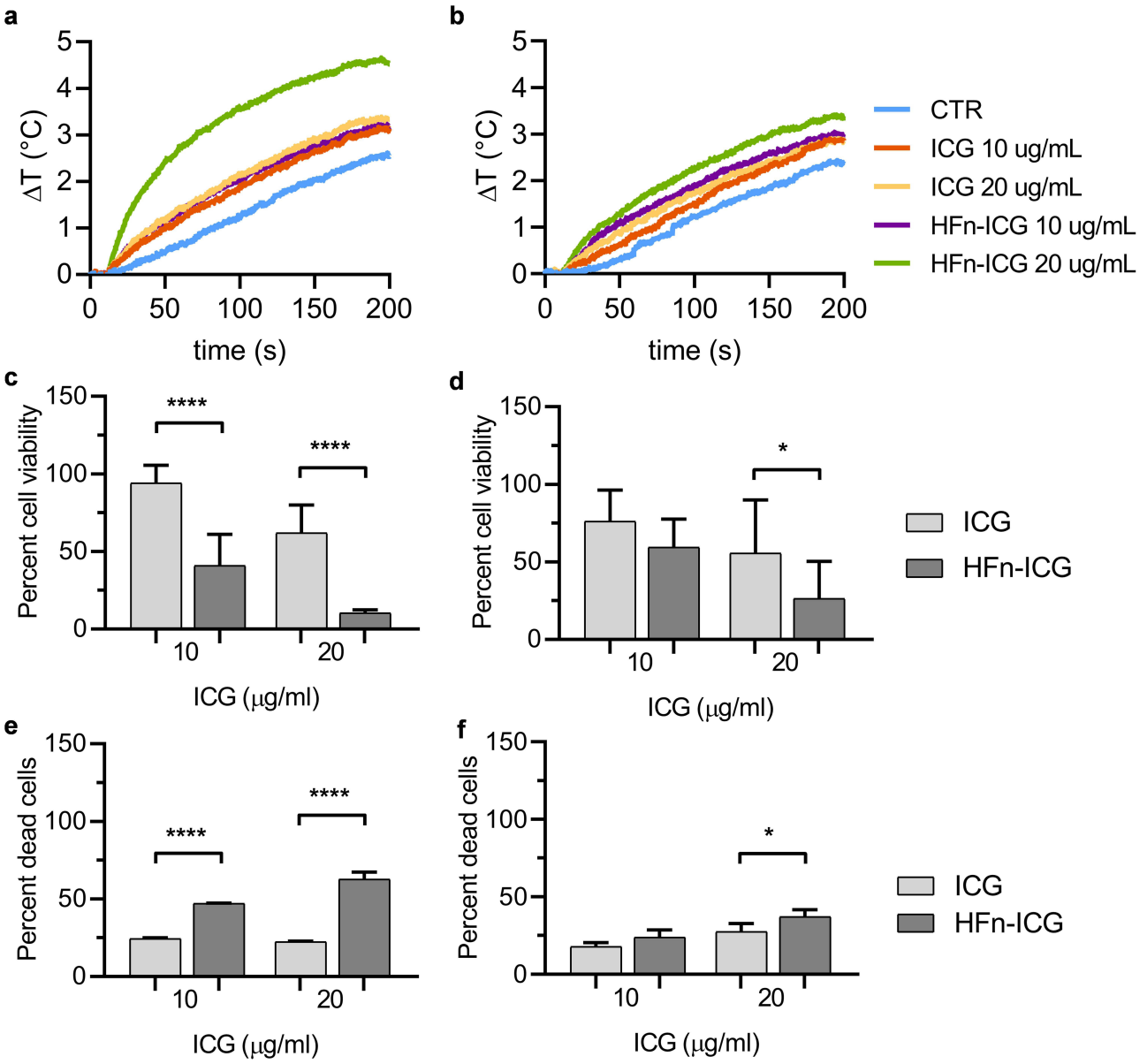

Figure 4 Temperature trends expressed as relative temperature increase (ΔT) of BT-474 (**a**) and HCC1937 (**b**) cells incubated with ICG and HFn-ICG at two different concentrations (10 and 20 μg/mL respectively) after irradiation (1W/cm^2, 3 min); cell viability (MTS assay) and dead cells percentage (7AAD marker by cytofluorimetry) assessment in BT-474 (**c** and **e**) and HCC1937 (**d** and **f**) after incubation with ICG (light gray) and HFn-ICG (dark gray) at two different concentrations. Statistical analysis was done by ordinary one-way ANOVA. *p<0.05, ****p<0.0001.

irradiation, only BT-474 treated with HFn-ICG exhibited remarkably altered morphology. In ICG-treated BT-474 and HCC1937 cells, signs of toxicity were observed only 24 h later. These data further confirmed the higher and faster cytotoxicity of HFn TfR1 mediated uptake in BT-474 cells, as previously reported.

No effects were observed in irradiated untreated cells (CTR$^+$), confirming the good tolerability of the laser setup. To help us distinguish the endogenous H-Fn from the uptaken HFn, we incubated cells with HFn-FITC and irradiated them as done for ICG-treated cells (Figure S7a and b). Here, only a slight and non-significant increase in H-Fn was observed in non-irradiated cells, most likely due to the uptake of exogenous HFn. Interestingly, in irradiated cells incubated with HFn-FITC, no significant increase in H-Fn was observed, further confirming that the presence of ICG is essential for oxidative stress, which consequently activates the described H-Fn-based mechanism of cell defence.

Table 2 Temperature Data of BT-474 Cells Irradiated with Increasing Concentrations of ICG and HFn-ICG

Sample	T_{in} (°C)	T_{max} (°C)	ΔT_{max} (°C)
CTRL	24.0 ± 0.4	26.6 ± 0.6	2.6 ± 0.2
ICG 10 μg/mL	24.1 ± 0.1	27.2 ± 0.7	3.2 ± 0.6
ICG 20 μg/mL	23.8 ± 0.4	27.1 ± 0.6	3.4 ± 0.2
HFn-ICG 10 μg/mL	24.7 ± 0.1	27.9 ± 0.3	3.2 ± 0.3
HFn-ICG 20 μg/mL	24.5 ± 0.1	29.1 ± 0.5	4.6 ± 0.5

Table 3 Temperature Data of HCC1937 Cells Irradiated with Increasing Concentrations of ICG and HFn-ICG

Sample	T_{in} (°C)	T_{max} (°C)	ΔT_{max} (°C)
CTRL	25.7 ± 0.6	28.2 ± 0.4	2.4 ± 0.2
ICG 10 μg/mL	24.2 ± 0.1	27.1 ± 0.4	2.9 ± 0.4
ICG 20 μg/mL	25.2 ± 0.5	28.1 ± 0.3	2.9 ± 0.2
HFn-ICG 10 μg/mL	24.5 ± 0.2	27.6 ± 0.2	3.1 ± 0.1
HFn-ICG 20 μg/mL	24.6 ± 0.1	28.0 ± 0.2	3.4 ± 0.1

Finally, to identify the irradiation-induced products of ICG, which could underlie the toxicity of the dye, we analyzed free and nanoformulated ICG sample solutions using UHPLC-MS/MS before and after irradiation. In Figure 6a, the chromatographic profile of the ICG sample solution in PBS buffer is shown. The target molecule was characterized by a Rt of 3 min after UHPLC separation and detection in ESI positive mode, as reported in the small chromatogram on the right-hand side of the panel. Furthermore, the MS/MS spectrum of the ICG moiety was obtained and is displayed on the left side of the same panel. The most abundant product ions of the parent compound occurred at m/z 422, 382.2 and 330.2; the tentative structures of these product ions are shown in Figure 6a: the most representative fragment ion of ICG that occurs at m/z 330.2 may originate from cleavage of the C–C bond of the benzoindole group linked to the alkene chain. C-C cleavage is mostly due to double bonds in the unsaturated chain. The fragment ion at m/z 330.2 was therefore obtained in both neutral loss and product ion scans to confirm the presence or absence of ICG after irradiation. For the selective detection of ICG in both formulations (free ICG and HFn-ICG), a neutral loss at m/z 330.2 was used. The UHPLC-MS/MS profiles of HFn-ICG and irradiated HFn-ICG are shown as small chromatograms in Figures 6b and c, respectively. The neutral loss scan performed at m/z 330.2 enabled the selective detection of the ion at m/z 753.0 as the protonated molecular ion of ICG in the non-irradiated HFn-ICG (Figure 6b, large chromatogram). This methodology enabled us to demonstrate the absence of ICG after irradiation (Figure 6c, large chromatogram). Mass spectrometry was used to confirm that HFn-ICG was degraded after irradiation, and different dye fractions were formed, similar to those observed for free ICG.

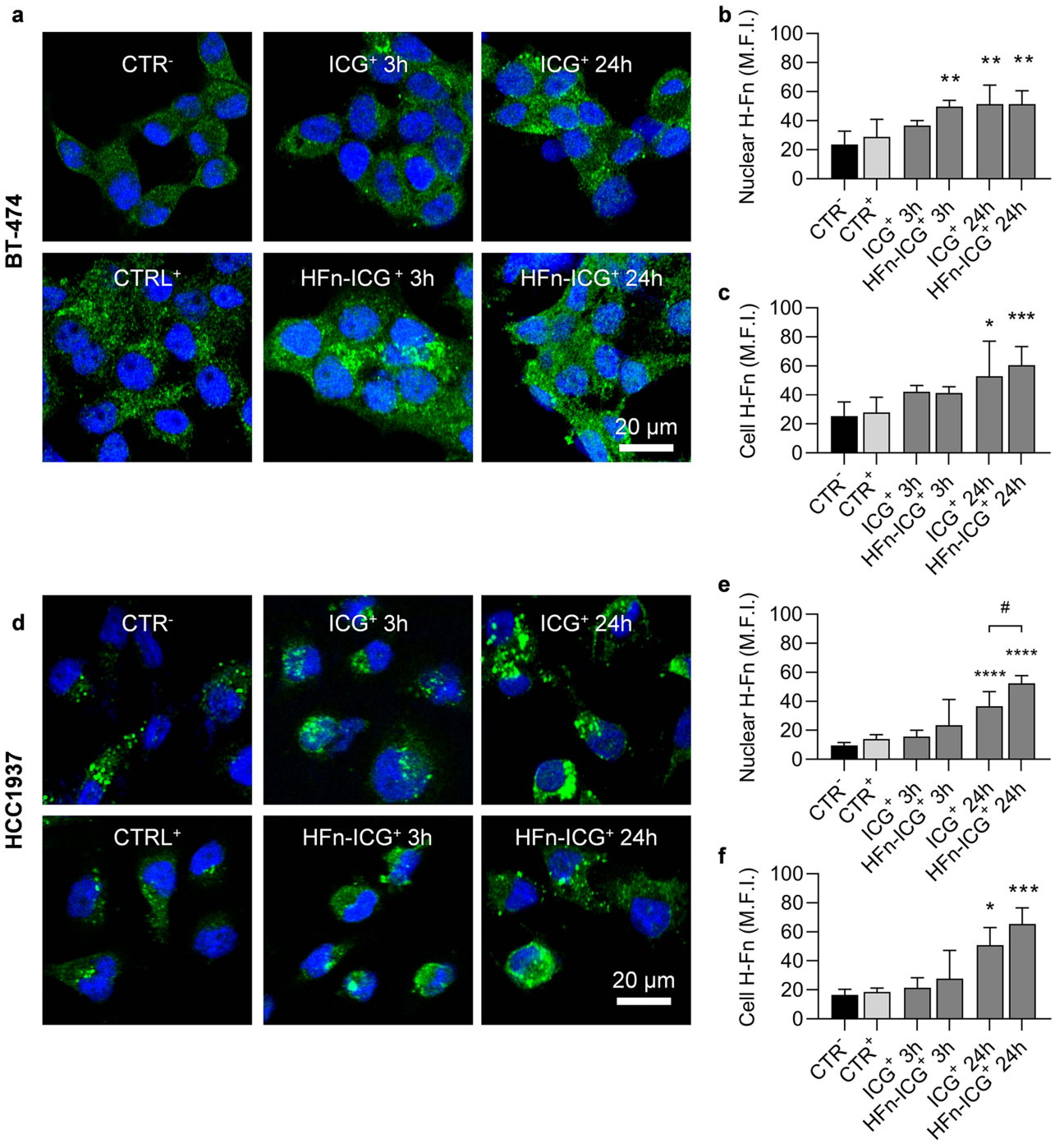

Figure 5 Confocal microscopy images of BT-474 and HCC1937 cells (**a** and **d**) were used to calculate nuclear (**b** and **e**) and cytoplasmic (**c** and **f**) H-Fn expression 3h and 24h after irradiation of cells incubated with equivalent concentrations of 10 µg/mL of ICG. Untreated non-irradiated and irradiated cells ($CTR^-$and CTR^+ respectively); ICG and HFn-ICG treated non-irradiated cells (ICG^-, $HFn\text{-}ICG^-$ respectively); ICG and HFn-ICG treated irradiated cells (ICG^+ and $HFn\text{-}ICG^+$ respectively). M.F.I.= Mean Fluorescence Intensity. Statistical analysis was done by ordinary one-way ANOVA. *p<0.05, **p<0.01, ***p<0.001, ****p<0.0001 against relative CTR groups; #p<0.05 as indicated.

Conclusion

In this study, we confirmed that, through a Trojan horse-like delivery mechanism that we unveiled, HFn-ICG significantly improved PDT efficacy in two different BC cell lines. In line with the highly conservative approaches that are emerging in clinics, in future in vivo experiments, we will apply repeated low-energy irradiation sessions to exploit PDT

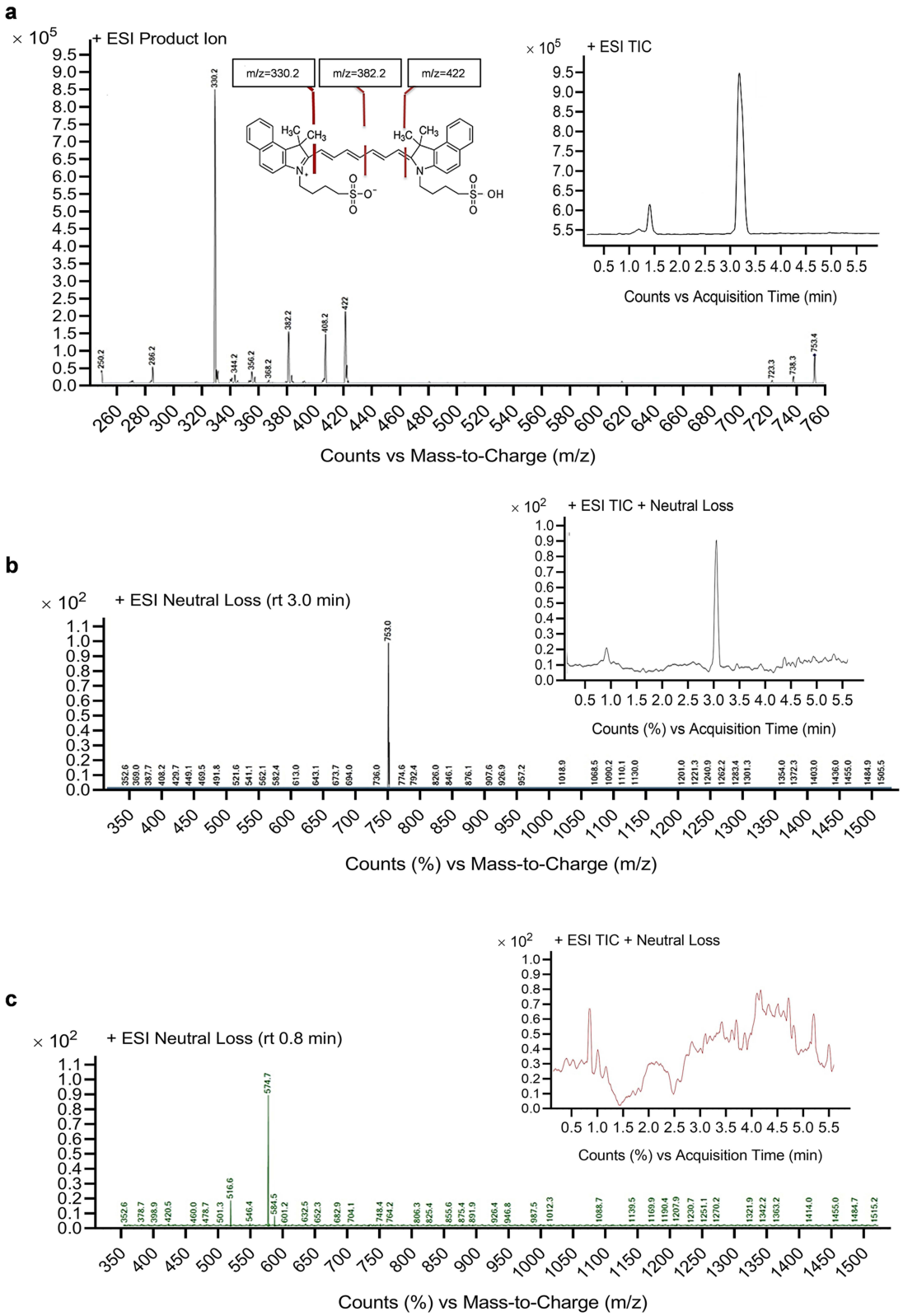

Figure 6 UHPLC-MS/MS profile of free ICG and its MS/MS spectrum (**a**); UHPLC-MS/MS profile and relative neutral loss scans performed at m/z 330 of HFn-ICG (**b**) and irradiated HFn-ICG (**c**).

advantages without incurring off-target PTT side effects related to a high laser power. Moreover, it will be of great interest to study the immunostimulatory potential of PDT by evaluating cytokine production as well as T-cell recruitment both in the primary tumor and in the metastatic foci typical of several TNBC in vivo models.

Abbreviations

PDT, photodynamic therapy; PTT, photothermal therapy; ICG, indocyanine green; PS, photosensitizer; HFn, recombinant heavy ferritin; H-Fn, endogenous heavy ferritin; Fn, human protein ferritin; TfR1, transferrin receptor 1; BC, breast cancer; FDA, Food and Drug Administration; NIR, near-infrared; ROS, reactive oxygen species; DNA, Deoxyribonucleic acid; ICD, immunogenic cell death; NPs, nanoparticles; EPR, enhanced permeability and retention; ATCC, American Type Culture Collection; LGC, Laboratory of the Government Chemist; DMEM, Dulbecco's Modified Eagle Medium; HG, High Glucose; FBS, fetal bovine serum; EDTA, Ethylenediaminetetraacetic Acid; MW, multiwell; min, minutes; h, hours; fps, frames per second; ROI, region of interest; MTS, MTS (3-(4,5-dimethylthiazol-2-yl)-5-(3-carboxymethoxyphenyl)-2-(4-sulfophenyl)-2H-tetrazolium); PFA, paraformaldehyde; RT, room temperature; BSA, Bovine Serum Albumin; GS, Goat Serum; O/N, Overnight; PBS, Phosphate-Buffered Saline; IPTG, isopropyl β-d-1-tiogalactopiranoside; LB, Luria Bertani; DEAE, Diethylaminoethyl cellulose; LPS, endotoxins/lipopolysaccharides; TEM, transmission electron microscopy; LAL, Limulus amebocyte lysate; EU, endotoxin units; MWCO, molecular weight cutoff; LC, loading capacity; 7-AAD, 7-aminoactinomycin D; M.F.I., mean fluorescence intensity; UHPLC-MS/MS, Ultra High Performance tandem Mass Spectrometry; ESI-MS/MS, electrospray ion source tandem mass spectrometry; CID, collisional-induced dissociation; Rt, retention time.

Data Sharing Statement

Availability of data and materials: Raw data are available in a publicly accessible repository after publication (https://doi.org/10.13130/RD_UNIMI/WYJ0FB).

Acknowledgments

The research leading to these results received funding from AIRC under IG 2017—ID20172 P.I. Corsi and IG2022-ID27107 P.I. Mazzucchelli, and from the European Research Council (ERC) under the European Union's Horizon 2020 research and innovation program (Grant agreement No. 759159-P.I. Saccomandi). We acknowledge the University of Milan for M. S. PhD fellowship and AIRC IG2022-ID27107 P.I. Mazzucchelli for L.S. post-doctoral position. We acknowledge the University of Milan for support in open access publication. Finally, we thank Prof. Nica Borgese for her precious contribution in improving the English language and writing flow of the manuscript thoroughly.

The graphical abstract was created with Biorender.com.

Author Contributions

All authors made a significant contribution to the work reported, whether that is in the conception, study design, execution, acquisition of data, analysis and interpretation, or in all these areas; took part in drafting, revising or critically reviewing the article; gave final approval of the version to be published; have agreed on the journal to which the article has been submitted; and agree to be accountable for all aspects of the work.

Disclosure

The authors report no conflicts of interest in this work.

References

1. Kong C, Chen X. Combined photodynamic and photothermal therapy and immunotherapy for cancer treatment: a review. *IJN*. 2022;17:6427–6446. doi:10.2147/IJN.S388996
2. Li X, Lovell JF, Yoon J, Chen X. Clinical development and potential of photothermal and photodynamic therapies for cancer. *Nat Rev Clin Oncol*. 2020;17(11):657–674. doi:10.1038/s41571-020-0410-2
3. Asadi S, Bianchi L, De Landro M, Korganbayev S, Schena E, Saccomandi P. Laser-induced optothermal response of gold nanoparticles: from a physical viewpoint to cancer treatment application. *J Biophotonics*. 2021;14(2):e202000161. doi:10.1002/jbio.202000161

4. Kou J, Dou D, Yang L. Porphyrin photosensitizers in photodynamic therapy and its applications. *Oncotarget*. 2017;8(46):81591–81603. doi:10.18632/oncotarget.20189
5. Sternberg ED, Dolphin D, Brückner C. Porphyrin-based photosensitizers for use in photodynamic therapy. *Tetrahedron*. 1998;54(17):4151–4202. doi:10.1016/S0040-4020(98)00015-5
6. Yorozu K, Kaibori M, Kimura S, et al. Experience with photodynamic therapy using indocyanine green liposomes for refractory cancer. *J Person Med*. 2022;12(7):1039. doi:10.3390/jpm12071039
7. Lin J, Lin LS, Chen DR, Lin KJ, Wang YF, Chang YJ. Indocyanine green fluorescence method for sentinel lymph node biopsy in breast cancer *Asian Journal of Surgery*. 2020; 43(12)1149–1153. doi:10.1016/j.asjsur.2020.02.003
8. Deng K, Hou Z, Deng X, Yang P, Li C, Lin J. Enhanced Antitumor Efficacy by 808 nm Laser-Induced Synergistic Photothermal and Photodynamic Therapy Based on a Indocyanine-Green-Attached W18O49 Nanostructure. *Adv Funct Mater*. 2015;25(47):7280–7290. doi:10.1002/adfm.201503046
9. Ming L, Cheng K, Chen Y, Yang R, Chen D. Enhancement of tumor lethality of ROS in photodynamic therapy. *Cancer Med*. 2021;10(1):257–268. doi:10.1002/cam4.3592
10. Li W, Yang J, Luo L, et al. Targeting photodynamic and photothermal therapy to the endoplasmic reticulum enhances immunogenic cancer cell death. *Nat Commun*. 2019;10(1):3349. doi:10.1038/s41467-019-11269-8
11. Sitia L, Sevieri M, Bonizzi A, et al. Development of tumor-targeted indocyanine green-loaded ferritin nanoparticles for intraoperative detection of cancers. *ACS Omega*. 2020;5(21):12035–12045. doi:10.1021/acsomega.0c00244
12. Truffi M, Fiandra L, Sorrentino L, Monieri M, Corsi F, Mazzucchelli S. Ferritin nanocages: a biological platform for drug delivery, imaging and theranostics in cancer. *Pharmacol Res*. 2016;107:57–65. doi:10.1016/j.phrs.2016.03.002
13. Sitia L, Galbiati V, Bonizzi A, et al. In vitro immunoreactivity evaluation of H-ferritin-based nanodrugs. *Bioconjugate Chem*. 2023;34(5):845–855. doi:10.1021/acs.bioconjchem.3c00038
14. Zhu Y, Zhu Y, Cao T, et al. Ferritin-based nanomedicine for disease treatment. *Med Rev*. 2023;3(1):49–74. doi:10.1515/mr-2023-0001
15. Deng G, Li Y, Liang N, et al. Ferritin in cancer therapy: a pleiotropic tumoraffin nanocage-based transport. *Cancer Med*. 2023;12(10):11570–11588. doi:10.1002/cam4.5778
16. Sevieri M, Pinori M, Chesi A, et al. Novel bioengineering strategies to improve bioavailability and in vivo circulation of H-ferritin nanocages by surface functionalization. *ACS Omega*. 2023;8(8):7244–7251. doi:10.1021/acsomega.2c07794
17. Mainini F, Bonizzi A, Sevieri M, et al. Protein-based nanoparticles for the imaging and treatment of solid tumors: the case of ferritin nanocages, a narrative review. *Pharmaceutics*. 2021;13(12):2000. doi:10.3390/pharmaceutics13122000
18. Khoshnejad M, Parhiz H, Shuvaev VV, Dmochowski IJ, Muzykantov VR. Ferritin-based drug delivery systems: hybrid nanocarriers for vascular immunotargeting. *J Control Release*. 2018;282:13–24. doi:10.1016/j.jconrel.2018.02.042
19. Li L, Fang CJ, Ryan JC, et al. Binding and uptake of H-ferritin are mediated by human transferrin receptor-1. *PNAS*. 2010;107(8):3505–3510. doi:10.1073/pnas.0913192107
20. The Human Protein Atlas. TFRC protein expression summary. Available from: https://www.proteinatlas.org/ENSG00000072274-TFRC. Accessed March 5, 2024.
21. Cui C, Cheng X, Yan L, et al. Downregulation of TfR1 promotes progression of colorectal cancer via the JAK/STAT pathway. *CMAR*. 2019;11:6323–6341. doi:10.2147/CMAR.S198911
22. Adachi M, Kai K, Yamaji K, et al. Transferrin receptor 1 overexpression is associated with tumour de-differentiation and acts as a potential prognostic indicator of hepatocellular carcinoma. *Histopathology*. 2019;75(1):63–73. doi:10.1111/his.13847
23. Chen F, Fan Y, Hou J, et al. Integrated analysis identifies TfR1 as a prognostic biomarker which correlates with immune infiltration in breast cancer. *Aging*. 2021;13(17):21671–21699. doi:10.18632/aging.203512
24. Rosager AM, Sørensen MD, Dahlrot RH, et al. Transferrin receptor-1 and ferritin heavy and light chains in astrocytic brain tumors: expression and prognostic value. *PLoS One*. 2017;12(8):e0182954. doi:10.1371/journal.pone.0182954
25. Palombarini F, Di Fabio E, Boffi A, Macone A, Bonamore A. Ferritin nanocages for protein delivery to tumor cells. *Molecules*. 2020;25(4):825. doi:10.3390/molecules25040825
26. Yin S, Davey K, Dai S, Liu Y, Bi J. A critical review of ferritin as a drug nanocarrier: structure, properties, comparative advantages and challenges. *Particuology*. 2022;64:65–84. doi:10.1016/j.partic.2021.04.020
27. Lee NK, Cho S, Kim IS. Ferritin – a multifaceted protein scaffold for biotherapeutics. *Exp Mol Med*. 2022;54(10):1652–1657. doi:10.1038/s12276-022-00859-0
28. Sevieri M, Silva F, Bonizzi A, et al. Indocyanine green nanoparticles: are they compelling for cancer treatment? *Front Chem*. 2020:8. doi:10.3389/fchem.2020.00535
29. Sevieri M, Sitia L, Bonizzi A, Truffi M, Mazzucchelli S, Corsi F. Tumor accumulation and off-target biodistribution of an indocyanine-green fluorescent nanotracer: an ex vivo study on an orthotopic murine model of breast cancer. *Int J Mol Sci*. 2021;22(4):1601. doi:10.3390/ijms22041601
30. Donohoe C, Senge MO, Arnaut LG, Gomes-da-Silva LC. Cell death in photodynamic therapy: from oxidative stress to anti-tumor immunity. *Bioch Bio Acta*. 2019;1872(2):188308. doi:10.1016/j.bbcan.2019.07.003
31. Orino K, Lehman L, Tsuji Y, Ayaki H, Torti SV, Torti FM. Ferritin and the response to oxidative stress. *Biochem J*. 2001;357(Pt 1):241–247. doi:10.1042/bj3570241
32. Park E, Chung SW. ROS-mediated autophagy increases intracellular iron levels and ferroptosis by ferritin and transferrin receptor regulation. *Cell Death Dis*. 2019;10(11):1–10. doi:10.1038/s41419-019-2064-5
33. Bellini M, Mazzucchelli S, Galbiati E, et al. Protein nanocages for self-triggered nuclear delivery of DNA-targeted chemotherapeutics in Cancer Cells. *J Control Release*. 2014;196:184–196. doi:10.1016/j.jconrel.2014.10.002
34. Colak B, Cihan MC, Ertas YN. 3D-printed, implantable alginate/cus nanoparticle scaffolds for local tumor treatment via synergistic photothermal, photodynamic, and chemodynamic therapy. *ACS Appl Nano Mater*. 2023;6(17):16076–16085. doi:10.1021/acsanm.3c03433
35. Milbrandt NB, Tsai YH, Cui K, et al. Combination d-amino acid and photothermal hydrogel for the treatment of prosthetic joint infections. *ACS Appl Bio Mater*. 2023;6(3):1231–1241. doi:10.1021/acsabm.2c01083
36. Long S, Xu Y, Zhou F, et al. Characteristics of temperature changes in photothermal therapy induced by combined application of indocyanine green and laser. *Oncol Lett*. 2019;17(4):3952–3959. doi:10.3892/ol.2019.10058

37. Millard M, Bernhard Y, Canilho N, et al. Enhanced stability and photothermal efficiency of Indocyanine Green J-aggregates by nanoformulation with Calix[4]arene for photothermal therapy of cancers. *Colloids Surf. B*. 2023;230:113516. doi:10.1016/j.colsurfb.2023.113516
38. Silva F, Sitia L, Allevi R, et al. Combined method to remove endotoxins from protein nanocages for drug delivery applications: the case of human ferritin. *Pharmaceutics*. 2021;13(2):229. doi:10.3390/pharmaceutics13020229
39. Chen R, Huang Y, Wang L, et al. Cetuximab functionalization strategy for combining active targeting and antimigration capacities of a hybrid composite nanoplatform applied to deliver 5-fluorouracil: toward colorectal cancer treatment. *Biomater Sci*. 2021;9(6):2279–2294. doi:10.1039/D0BM01904F
40. Han X, Fang W, Zhang T, et al. A facile phototheranostic nanoplatform integrating NIR-II fluorescence/PA bimodal imaging and image-guided surgery/PTT combinational therapy for improved antitumor efficacy. *J Mater Sci Technol*. 2022;130:208–218. doi:10.1016/j.jmst.2022.05.027
41. Sottani C, Grignani E, Cottica D, et al. Development and validation of a bioanalytical UHPLC-MS/MS method applied to murine liver tissue for the determination of indocyanine green loaded in H-ferritin nanoparticles. *Front Chem*. 2022;9. doi:10.3389/fchem.2021.784123
42. Shirata C, Kaneko J, Inagaki Y, et al. Near-infrared photothermal/photodynamic therapy with indocyanine green induces apoptosis of hepatocellular carcinoma cells through oxidative stress. *Sci Rep*. 2017;7(1):13958. doi:10.1038/s41598-017-14401-0
43. Tseng HC, Kuo CY, Liao WT, Chou TS, Hsiao JK. Indocyanine green as a near-infrared theranostic agent for ferroptosis and apoptosis-based, photothermal, and photodynamic cancer therapy. *Front Mol Biosci*. 2022;9. doi:10.3389/fmolb.2022.1045885
44. Tamai K, Mizushima T, Wu X, et al. Photodynamic therapy using indocyanine green loaded on super carbonate apatite as minimally invasive cancer treatment. *Mol Cancer Ther*. 2018;17(7):1613–1622. doi:10.1158/1535-7163.MCT-17-0788
45. Svaasand LO, Gomer CJ, Morinelli E. On the physical rationale of laser induced hyperthermia. *Laser Med Sci*. 1990;5(2):121–128. doi:10.1007/BF02031373
46. El-Daly SM, Gamal-Eldeen AM, Abo-Zeid MAM, Borai IH, Wafay HA, Abdel-Ghaffar ARB. Photodynamic therapeutic activity of indocyanine green entrapped in polymeric nanoparticles. *Photodiagn Photodyn Ther*. 2013;10(2):173–185. doi:10.1016/j.pdpdt.2012.08.003
47. Porcu EP, Salis A, Gavini E, Rassu G, Maestri M, Giunchedi P. Indocyanine green delivery systems for tumour detection and treatments Biotechnology Advances. 2016; 34(5) 768–789. doi:10.1016/j.biotechadv.2016.04.001
48. Dörner MH, Salfeld J, Will H, Leibold EA, Vass JK, Munro HN. Structure of human ferritin light subunit messenger RNA: comparison with heavy subunit message and functional implications. *Proc Natl Acad Sci*. 1985;82(10):3139–43.10.1073/pnas.82.10.3139. doi:10.1073/pnas.82.10.3139
49. Dawson M. For Parenteral Drug Products; 2017.
50. Huang P, Rong P, Jin A, et al. Dye-loaded ferritin nanocages for multimodal imaging and photothermal therapy. *Adv Mater*. 2014;26(37):6401–6408. doi:10.1002/adma.201400914